



# Highly selective formation of CO from domestic wastewater with Zero CO<sub>2</sub> emissions through solar energy catalysis

Zhonglian Shi<sup>a</sup>, Chao Li<sup>a</sup>, Niu Huang<sup>a,1</sup>, Ziyi Jiang<sup>a</sup>, Li Wang<sup>b</sup>, Yingping Huang<sup>b</sup>, Xin Ying Kong<sup>c</sup>, Po Keung Wong<sup>d</sup>, Liqun Ye<sup>a,b,\*,2</sup>

<sup>a</sup> College of Materials and Chemical Engineering, China Three Gorges University, Yichang 443002, Hubei, China

<sup>b</sup> Engineering Research Center of Eco-environment in Three Gorges Reservoir Region, Ministry of Education, China Three Gorges University, Yichang 443002, Hubei, China

<sup>c</sup> Division of Chemistry and Biological Chemistry, School of Physical and Mathematical Sciences, Nanyang Technological University, 21 Nanyang Link, 637371, Singapore

<sup>d</sup> School of Life Sciences, The Chinese University of Hong Kong, Shatin, Hong Kong, China

## ARTICLE INFO

### Keywords:

Domestic wastewater  
Photocatalysis  
<sup>1</sup>O<sub>2</sub> mild oxidation  
Cellulose conversion  
CO generation

## ABSTRACT

Utilizing two of the Earth's most abundant and inexhaustible resources, sunlight and domestic wastewater, to produce value-added CO presents an immense opportunity. Here, we present a novel strategy to selectively generate CO from domestic wastewater with the aid of concentrated solar power and high-entropy sulfide photocatalysts. Our designed system achieves an impressive CO yield of 35  $\mu\text{mol g}^{-1} \text{h}^{-1}$  with 100% selectivity, showcasing the feasibility of utilizing solar energy alone to drive the heat-promoted photoreaction. Mechanistic investigations divulged the generation of a non-radical <sup>1</sup>O<sub>2</sub> species with a moderate redox potential. This process enables mild oxidation of carbonaceous organic matter in domestic wastewater, rather than complete mineralization of carbonaceous organic matter and reducing greenhouse gas emissions such as CO<sub>2</sub> and CH<sub>4</sub> during organic matter degradation. The findings present an effective and promising approach for low-carbon wastewater treatment, highlighting the potential of CO production from wastewater through solar energy catalysis.

**Synopsis:** Through the rational design of the outdoor photocatalytic equipment, close to 100% selectivity from real domestic wastewater to CO gas was successfully achieved.

## 1. Introduction

Where humans settlements thrive, domestic wastewater is inevitably generated. For the treatment of domestic wastewater, wastewater treatment plants consume a significant 3% of the global electrical energy consumption. Meanwhile, the degradation of organic matter within the wastewater produces large amount and direct emission of greenhouse gases such as CH<sub>4</sub>, in which the greenhouse effect exhibited by CH<sub>4</sub> gas is stronger than that of CO<sub>2</sub>. [1–4] Traditionally, domestic wastewater treatments involve the use of aerobic activated sludge technology and anaerobic digestion, which involve complex oxidation processes. [5] Although anaerobic digestion can offset 20–30% of the energy and greenhouse gas costs of the activated sludge process, its digestion rate is

often sluggish, resulting in substantial time costs. In large-scale practical applications, microbial electrochemical system and anaerobic membrane bioreactor technology are often hindered by challenges such as membrane clogging, excessive energy consumption, high electrical resistance as well as elevated operating costs. [6–8] More importantly, the valuable energy present in the organic matter in the wastewater is wasted and left unutilized. [9–13] By tapping into the resource potential of domestic wastewater, we can simultaneously conserve energy and reduce greenhouse gas emissions, making a substantial contribution to the global carbon-neutral agenda. [14–16] Despite the tremendous potential of this technology, limited research has been conducted to convert the organic substances present in wastewater into value-added chemicals due to the insoluble and polymeric nature of certain organic

\* Correspondence to: College of Materials and Chemical Engineering, Key Laboratory of Inorganic Nonmetallic Crystalline and Energy Conversion Materials, China Three Gorges University, Yichang 443002, China.

E-mail address: [lqye@ctgu.edu.cn](mailto:lqye@ctgu.edu.cn) (L. Ye).

<sup>1</sup> [orcid.org/0000-0001-7860-9199](https://orcid.org/0000-0001-7860-9199)

<sup>2</sup> [orcid.org/0000-0001-6410-689X](https://orcid.org/0000-0001-6410-689X)

<https://doi.org/10.1016/j.apcatb.2023.123542>

Received 21 September 2023; Received in revised form 15 November 2023; Accepted 19 November 2023

Available online 22 November 2023

0926-3373/© 2023 Elsevier B.V. All rights reserved.

substances, making the conversion process has remained an enormous challenge thus far.

In this study, we have successfully achieved the selective conversion of organic matters present in domestic wastewater into a value-added chemical feedstock - carbon monoxide (CO) using a zero-energy solar catalysis approach, which serves as an effective and promising method for achieving carbon-neutral water treatment. This was achieved through photocatalysis, an effective process for harnessing and utilizing solar energy. The photoresponse of the photocatalysts and the separation efficiency of photogenerated electron-hole pairs are the pivotal factors to determine the performance and activity of photocatalysts. In the solar spectrum, ultraviolet (300–400 nm) constitutes for 3% while visible light (400–700 nm) and infrared region (>700 nm) account for 47% and 50% of sunlight, respectively. [17,18] Therefore, the development of novel nanomaterials with good photoresponse to a wide spectrum of sunlight is highly desirable as the utilization of solar energy can be greatly improved. Our recently reported high-entropy metal sulfide photocatalysts exhibit good photoresponse towards visible and infrared light, encompassing a range from 200 nm to 1400 nm. The enhanced photocatalytic material (NiCdCuFeCo) $S_x$  high-entropy sulfide, which is a high-entropy catalyst with strong surface relaxation and fast inter-metallic electron mobility, has been designed and prepared by employing a solid-solution strategy. [19] The developed high-entropy sulfide catalysts demonstrated excellent photoactivity toward selective conversion of cellulose, toilet paper scraps, and actual domestic wastewater into CO, utilizing peroxodisulfate sodium (PDS,  $Na_2S_2O_8$ ) as a mediator. The high-entropy sulfide effectively harness the previously wasted infrared light from sunlight, the infrared part of the light is mainly utilized in the form of heat, significantly enhancing the efficiency of solar energy utilization. In addition, the high-entropy effect and hysteresis diffusion effect of the high-entropy sulfide greatly improve the catalytic stability of the material, ensuring a well-balanced activity-stability relationship. [20–22] In this study, we extend the application of high-entropy sulfide catalysts to selectively convert the organics in real wastewater into CO. For large-scale solar-driven selective conversion of organics in wastewater, a careful design the reactors is essential. Herein, we employed Fresnel lens to concentrate sunlight for attaining a desired temperature to facilitate the conversion of organic matter in real domestic wastewater. The feasibility of harnessing sunlight to provide both solar and thermal energy to drive the selective generation of CO from domestic wastewater was demonstrated in this study.

## 2. Materials and methods

### 2.1. Synthesis of high-entropy sulfides

The (NiCdCuFeCo) $S_x$  was synthesized by a facile precipitation solvothermal method. [19] Equimolar amounts of metal salts (1 mmol each) including  $Cd(Ac)_2 \cdot 2 H_2O$ ,  $(Ni(Ac)_2 \cdot 4 H_2O)$ ,  $(Co(NO_3)_2 \cdot 6 H_2O)$ ,  $(Cu(Ac)_2 \cdot H_2O)$ ,  $(Fe(NO_3)_3 \cdot 9 H_2O)$  and 0.4 g  $Na_2S \cdot 9 H_2O$  were dispersed in 35 mL of ethylene glycol with vigorous stirring. The resulting mixture was transferred to a 50 mL Teflon-lined stainless steel autoclave for solvothermal reaction to carry out at 150 °C for 16 h. After naturally cooling to room temperature, the precipitate was collected by centrifugation and washed with deionized water and ethanol for six times before drying at 60 °C for 12 h. The characterization of (NiCdCuFeCo) $S_x$  is described in results and discussion. The synthesis of control samples and characterization methods are described in the [Supplementary Information](#).

### 2.2. Domestic wastewater conversion test

The photocatalytic conversion of CO from cellulose was studied at room temperature and atmospheric pressure. Generally, 50 mL deionized water, 0.025 g catalyst, 0.05 g cellulose, and 0.06 g  $Na_2S_2O_8$  (PDS)

were added to a glass reactor. The mixture was thoroughly stirred and argon was employed to purify the air in the reactor. A Xenon arc lamp (pls-sce300c, Beijing Perfect Light Technology Co., LTD, China) ( $\lambda \geq 420$  nm, 300 mW  $cm^{-2}$ ) was employed as the light source. Under the light irradiation, gas sample of 1 mL was extracted with a syringe at every 30 min interval. In the actual domestic wastewater conversion, a Fresnel lens in 345 mm  $\times$  345 mm dimension was used to concentrate solar light and to provide necessary temperature for photocatalytic conversion of domestic wastewater. During the experiments, the window of the vessel overlaps with the focal point of the Fresnel lens to ensure maximum utilization of solar energy.

### 2.3. Analytical methods

The yield of gas products was detected by gas chromatograph (GC 9790II, Zhejiang Fuli Analytical Instrument Co., LTD, China) equipped with a flame ionization detector (FID). The amount of CO and  $C_2H_4$  was evaluated according to the fitted standard curve. The concentration of active species were quantified by a high performance liquid chromatography (HPLC) and a UV-Vis spectrophotometer detector. Detailed HPLC analytical methods are listed in the [Supplementary Information](#).

## 3. Results and discussion

### 3.1. Material characterization

The X-ray diffraction (XRD) pattern of our developed (NiCdCuFeCo) $S_x$  is shown in Fig. 1a. The XRD patterns of other samples including (CdNiCuCoFe) $S_x$ , (CdCuNiFe) $S_x$ , (CdCuFe) $S_x$ , (CdCu) $S_x$ , and CdS are shown in Fig. S1 in the [Supporting Information](#). As delineated in Fig. 1a, our synthesized (NiCdCuFeCo) $S_x$  exhibited three main diffraction peaks at  $2\theta = 26^\circ$ ,  $44^\circ$ , and  $52^\circ$ , which can be attributed to the (002), (110), and (112) crystal planes of the face-centred cubic (fcc) phase, respectively. Additionally, the experimental XRD matches well with the simulated XRD, indicating the successful formation of (NiCdCuFeCo) $S_x$  with high purity. Since no XRD diffraction peak was observed for Ni, Cd, Cu, Fe, Co or metal sulfide, it indicates the formation of a single-phase solid solution structure without segregation. In comparison to the XRD peaks of cadmium sulfide (CdS) in the database (standard card PDF#77–2306) (Fig. S2), (NiCdCuFeCo) $S_x$  exhibits a slight shift in the diffraction peak to a lower angle in the fcc phase due to the doping of Fe, Cu, Co, and Ni atoms and the resulting lattice distortion caused by the high-entropy effect. The lattice distortion of (NiCdCuFeCo) $S_x$  led to the weakening and broadening of the XRD diffraction peaks. [23] The XRD patterns of (NiCdCuFe) $S_x$ , (CdCuFe) $S_x$  and (CdCu) $S_x$  (Fig. S1) exhibited characteristic peaks correspond to the (002), (110), and (112) planes of the fcc phase, indicating that the crystal structure of fcc can still be well-maintained even if there is an alteration in the number of elements. For comparison, we also synthesized various metal sulfides as control samples (Fig. S3–7). Scanning electron microscopy (SEM) and transmission electron microscopy (TEM) images clearly show that (NiCdCuFeCo) $S_x$  is of two-dimensional nanosheet morphology (Fig. S8). High-resolution TEM (HR-TEM) images (Fig. 1b) disclose the single-crystal structure of (NiCdCuFeCo) $S_x$  with lattice spacings of 0.32 nm, 0.20 nm and 0.19 nm (Fig. S9) associated with sulfur cadmium ore 0.34 nm - (002), 0.21 nm - (110) and 0.18 nm - (112) crystal plane spacings, respectively. The (002) plane spacing of the (NiCdCuFeCo) $S_x$  crystal region in Fig. 2b is 0.32 nm. The fast Fourier transform (FFT) mode of the selected region and the corresponding lattice spacing distribution are shown in Fig. 1c. Charge density of the metallic elements in (NiCdCuFeCo) $S_x$  is illustrated in Fig. 1d. The high-angle annular dark field transmission electron microscopy (HAADF-STEM) elemental images (Fig. 1e) suggest the uniform distribution of six different elements including Ni, Cd, Cu, Fe, Co, and S without obvious elemental segregation and phase separation was observed. In addition, the elemental composition of (NiCdCuFeCo) $S_x$  was further investigated using

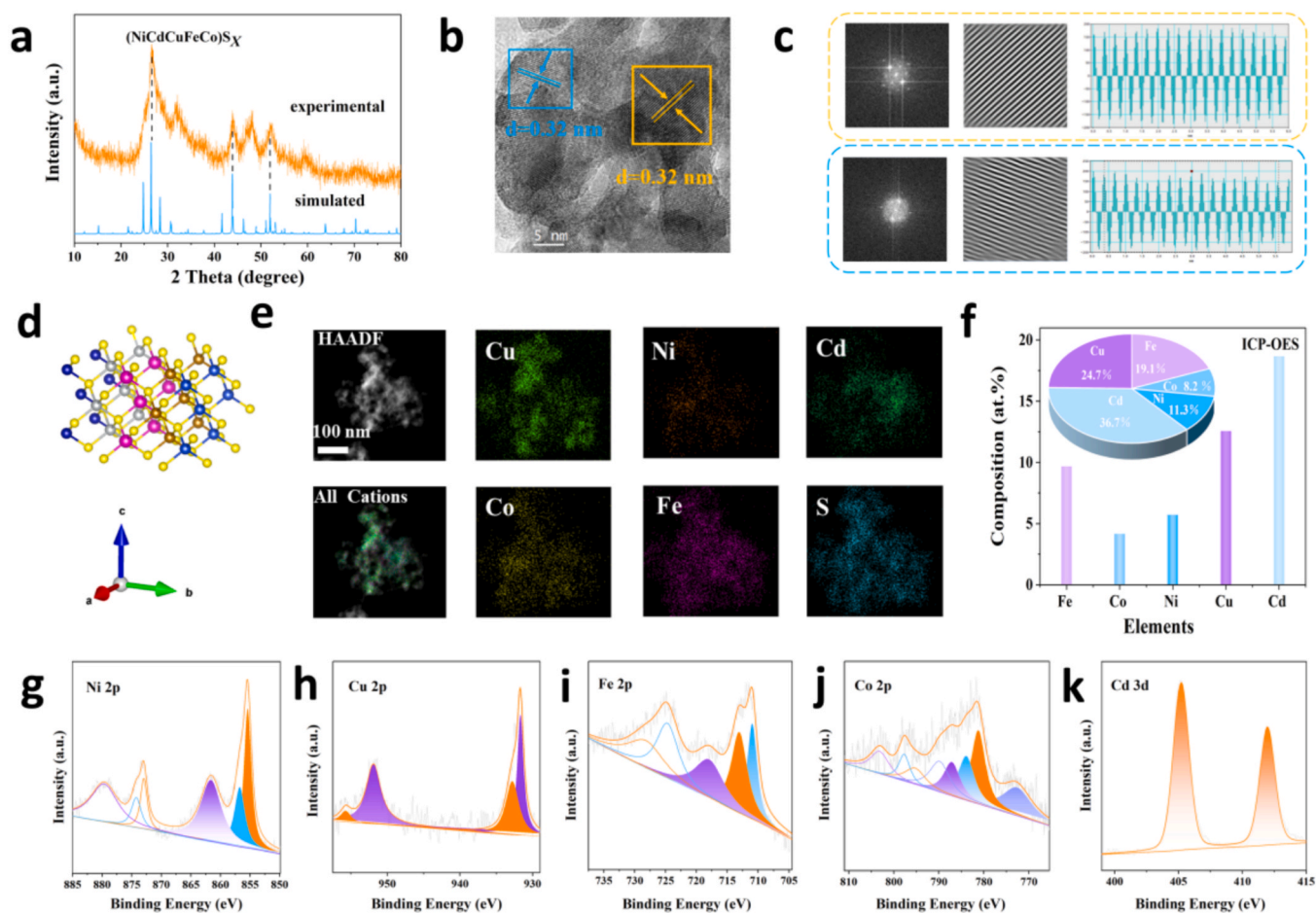


**Fig. 1.** Morphological and structural characterization of (NiCdCuFeCo)<sub>S<sub>x</sub></sub>. (a) Experimental and simulated XRD patterns of (NiCdCuFeCo)<sub>S<sub>x</sub></sub>. (b) and (c) HRTEM images of (NiCdCuFeCo)<sub>S<sub>x</sub></sub> and Fast Fourier Transform (FFT) pattern and the corresponding lattice spacing distribution of the selected regions. (d) Charge densities of metallic elements in (NiCdCuFeCo)<sub>S<sub>x</sub></sub> where blue: Cu atoms, pink: Cd atoms, brown: Fe atoms, navy: Co atoms, gray: Ni atoms, and yellow: S atoms. (e) HAADF-STEM mapping images of (NiCdCuFeCo)<sub>S<sub>x</sub></sub>. (f) Overall atomic percentages of metals in the (NiCdCuFeCo)<sub>S<sub>x</sub></sub> as determined by ICP—OES. The high-resolution (g) Ni 2p, (h) Cu 2p, (i) Fe 2p, (j) Co 2p, and (k) Cd 3d XPS spectra of the (NiCdCuFeCo)<sub>S<sub>x</sub></sub>.

inductively coupled plasma emission spectroscopy (ICP-OES) (Fig. 1f) and x-ray photoelectron spectroscopy (XPS). While ICP-OES spectroscopy provides information on the average composition of (NiCdCuFeCo)<sub>S<sub>x</sub></sub>, X-ray photoelectron spectroscopy (XPS) is more sensitive to the surface region of the sample. The findings from both ICP-OES and XPS are consistent with the composition of (NiCdCuFeCo)<sub>S<sub>x</sub></sub>, with a calculated mixing entropy of  $\Delta S > 1.50$  R (Tables S1). We further investigated the surface composition of (NiCdCuFeCo)<sub>S<sub>x</sub></sub> using XPS spectroscopy. The survey XPS spectrum and high-resolution S2p spectrum of (NiCdCuFeCo)<sub>S<sub>x</sub></sub> are shown in Fig. S10. Fig. 1g-k show the presence of Fe<sup>2+</sup>/Fe<sup>3+</sup>, Co<sup>0</sup>/Co<sup>2+</sup>/Co<sup>3+</sup>, Ni<sup>2+</sup>/Ni<sup>3+</sup>, Cu<sup>+</sup>/Cu<sup>2+</sup>, and Cd<sup>2+</sup> species in (NiCdCuFeCo)<sub>S<sub>x</sub></sub>. In addition, further Auger electron spectroscopy (AES) was performed to confirm the Cu<sup>+</sup> site (Fig. S11). The high-resolution Fe 2p, Cu 2p, Ni 2p, Co 2p, and Cd 3d spectra of the unitary metal sulfide samples (Fig. S3-7) were also recorded to provide more information on the electron interaction among the metal elements in (NiCdCuFeCo)<sub>S<sub>x</sub></sub>. It was observed the binding energies for Ni, Cd, Co, and Fe in (NiCdCuFeCo)<sub>S<sub>x</sub></sub> were shifted towards higher binding energy in comparison to NiS, CdS, CoS, and Fe<sub>3</sub>S<sub>4</sub>, respectively (Fig. S12 a-d). On the contrary, the binding energy for Cu in (NiCdCuFeCo)<sub>S<sub>x</sub></sub> shifted towards lower binding energy when compared with CuS (Fig. S12 e), demonstrating that Cu atom in (NiCdCuFeCo)<sub>S<sub>x</sub></sub> served as the electron acceptor. The findings above suggest the electron transfer between each metal atom in (NiCdCuFeCo)<sub>S<sub>x</sub></sub>.

### 3.2. Performance evaluation

Domestic wastewater contains various debris from our daily lives, including feces, toilet paper scraps, fats, food residues, detergents, and others. From a chemical perspective, one cubic meter of domestic wastewater contains several hundred grams of carbon-rich organic matter, with cellulose being a prevalent organic component. Hence, cellulose serves as a suitable model for studying the conversion of domestic wastewater into value-added CO. [24] In this study, we utilized cellulose as a research subject to investigate resource conversion under room temperature and ambient pressure under simulated sunlight irradiation. Based on the gas chromatography (GC) analysis, CO was found as the main product from cellulose conversion (Fig. 2a). Notably, (NiCdCuFeCo)<sub>S<sub>x</sub></sub> demonstrated excellent catalytic selectivity for cellulose conversion compared to other metal sulfides with relatively simpler compositions (i.e., consisting of one to four elements) (Fig. S13). Unary, binary, and ternary metal sulfides composed of only a few metal elements lack the extensive compositional tunability exhibited by (NiCdCuFeCo)<sub>S<sub>x</sub></sub>, which contains multiple metal elements. According to Sabatier's principle, optimal adsorption of intermediates can be achieved by (NiCdCuFeCo)<sub>S<sub>x</sub></sub>, thereby promoting the catalytic activity of cellulose conversion. [25–27] Importantly, (NiCdCuFeCo)<sub>S<sub>x</sub></sub> also exhibits excellent cyclic stability. (Fig. 2b, Fig. S14). For the control experiments with only (i) light + catalyst, (ii) light + PDS, and (iii) PDS + catalyst, the amount of CO generated from cellulose was negligible. However, for the case with co-existence of light + catalyst + PDS, the

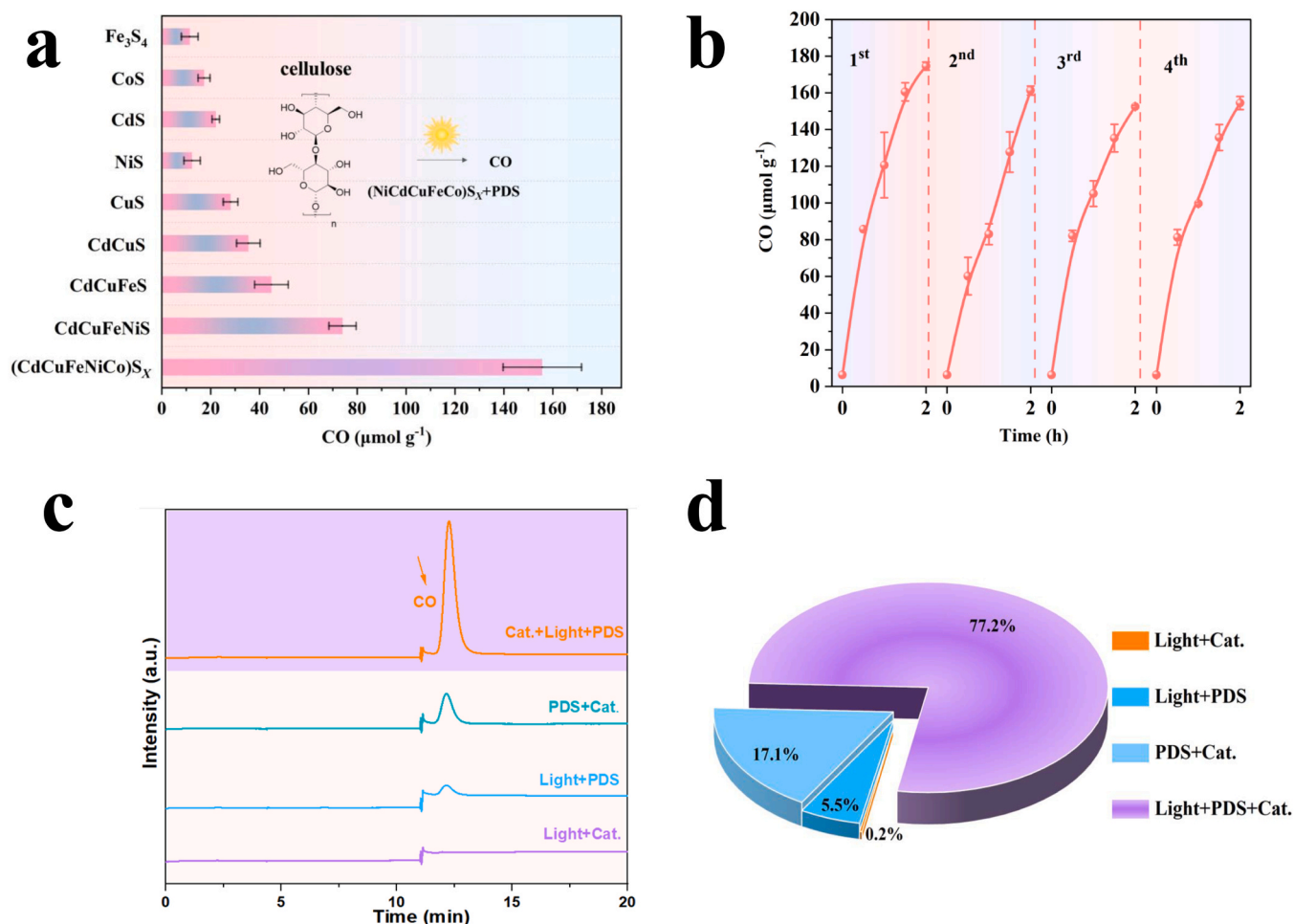


**Fig. 2.** Cellulose conversion over (NiCdCuFeCo)S<sub>x</sub> via solar energy catalysis. (a) The amount of CO produced over different sulfide-based catalysts. Reaction conditions: [cellulose] = 1 g L<sup>-1</sup>, [PDS] = 1.2 g L<sup>-1</sup>, [catalyst] = 0.5 g L<sup>-1</sup>, Xenon arc lamp intensity 0.96 W. (Subsequent experiments light intensity is 0.96 W unless otherwise stated) (b) Cyclic robustness tests of carbon monoxide production by (NiCdCuFeCo)S<sub>x</sub>. (c) Gas chromatographic diagram of CO gas produced under different reaction conditions. (d) The pie chart shows the respective percentage of CO gas produced under four different conditions: light + Cat. (yellow), light + PDS (light blue), PDS + Cat. (dark blue), light + PDS + Cat. (purple).

efficiency of cellulose conversion into CO was greatly boosted (Fig. 2c). It is thus clear that light, catalyst, and PDS are the prerequisites for the selective conversion of cellulose into CO. To achieve efficient solar energy utilization, a photocatalyst that is responsive to broad solar spectrum is essential. The DRS spectrum of (NiCdCuFeCo)S<sub>x</sub> clearly shows that its absorption edge is red-shifted and is able to fully utilize the heat from sunlight (Fig. S15). After 15 min of irradiation under Xenon arc lamp, the highest temperature of the reaction system in the presence of (NiCdCuFeCo)S<sub>x</sub>, CdS, and in the absence of catalyst were measured to be 41.2 °C, 29.1 °C and 25.8 °C, respectively (Fig. S16). This suggests the pivotal role of (NiCdCuFeCo)S<sub>x</sub> to effectively introduce thermal effects to the reaction system, in which the increase in temperature accelerated the kinetic process of the reaction (Fig. S17). The relative percentages of CO generation were 0.2%, 5.5%, 17.1%, and 77.2% for the reaction conditions of (i) light + catalyst, (ii) light + PDS, (iii) PDS + catalyst, and (iv) light + catalyst + PDS, respectively. This result indicates that the light-driven thermal effect and (NiCdCuFeCo)S<sub>x</sub> exhibit a synergistic effect in activating PDS, thereby enhancing the rate of CO generation (Fig. 2d). In addition to enhanced catalyst spectral absorption, the separation of photogenerated carriers plays a key factor in determining photocatalytic activity. Notably, (NiCdCuFeCo)S<sub>x</sub> exhibits a small radius of the Nyquist curve arc (Fig. S18), indicating unimpeded electron transfer and enhanced reaction kinetics in the photocatalytic reaction. Transient photocurrent response (TPR) and

photoluminescence (PL) were also performed in order to further investigate the separation of their photogenerated carriers (Fig. S19, Fig. S20). In summary, (NiCdCuFeCo)S<sub>x</sub> demonstrates excellent light absorption performance and enhanced separation of electron-hole pairs.

### 3.3. Mechanism analysis

The analyses presented above elucidates the process of cellulose resource utilization over (NiCdCuFeCo)S<sub>x</sub> photocatalyst. However, the underlying mechanism for the selective generation of CO gas from cellulose remains unclear. To investigate the contribution of each reactive species produced in the (NiCdCuFeCo)S<sub>x</sub> system under simulated sunlight irradiation, we systematically performed a series of radical quenching experiments (Fig. 3a, Fig. S21). Compared to the blank test, the addition of tert-butanol (TBA) as a •OH quencher did not significantly inhibit CO gas production ( $k_{\bullet\text{OH}, \text{TBA}} = 3.8\text{--}7.6 \times 10^8 \text{ M}^{-1} \text{ s}^{-1}$ ). [28,29] On the other hand, the presence of methanol (MeOH) to serve as a quencher for SO<sub>4</sub><sup>•-</sup> and •OH ( $k_{\text{SO}_4^{\bullet-}, \text{MeOH}} = 1.6\text{--}7.8 \times 10^7 \text{ M}^{-1} \text{ s}^{-1}$ ;  $k_{\bullet\text{OH}, \text{MeOH}} = 1.2\text{--}2.8 \times 10^9 \text{ M}^{-1} \text{ s}^{-1}$ ) greatly inhibit the CO production, mainly due to the masking of photogenerated holes rather than free radical quenching. To further determine the role of SO<sub>4</sub><sup>•-</sup>, semi-quantification of the generated SO<sub>4</sub><sup>•-</sup> was performed using p-hydroxybenzoic acid (PHBA) as a probe, revealing a SO<sub>4</sub><sup>•-</sup> concentration of only 7.0 μM (Fig. 3b, Fig. S22). Additionally, terephthalic acid



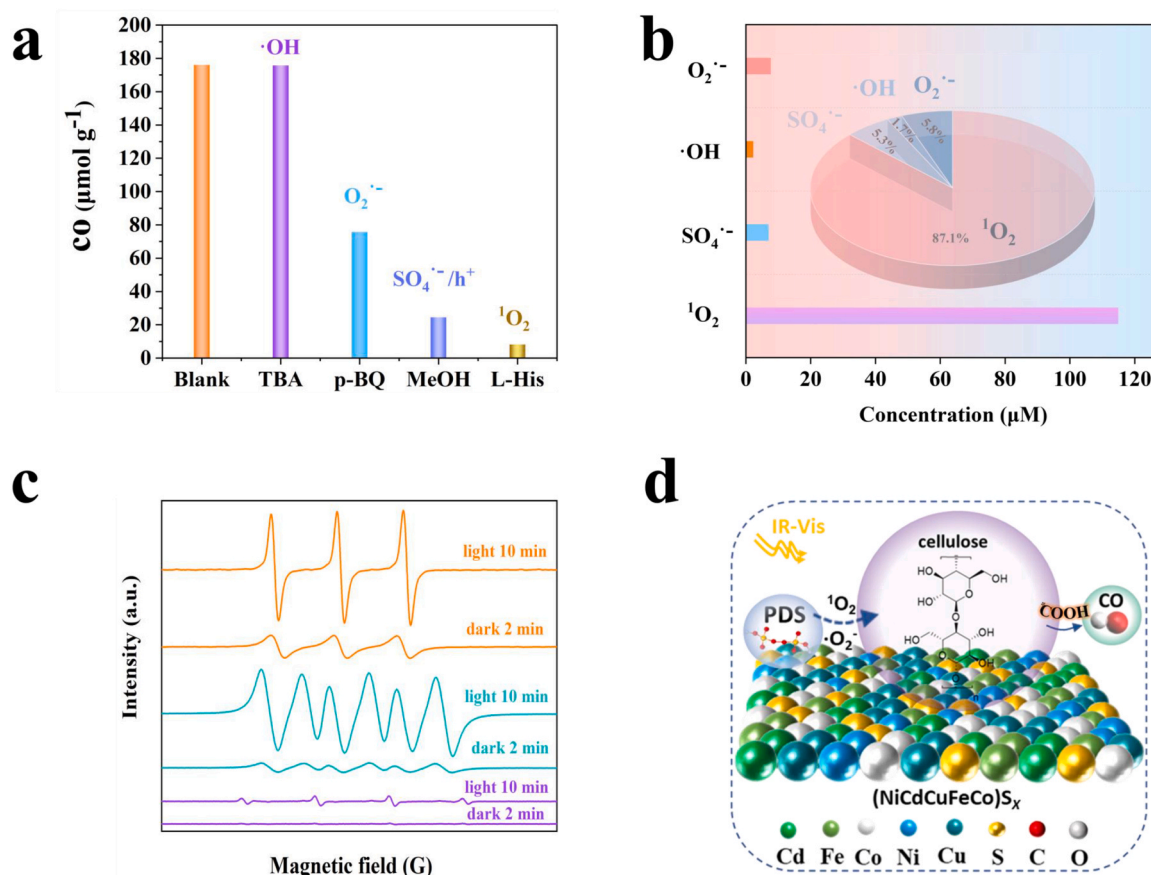


**Fig. 3.** Mechanism analysis of the selective conversion of domestic wastewater via solar energy catalysis. (a) The amount of CO produced by cellulose in the presence of different radical scavengers, including MeOH, TBA, L-His, and p-BQ. Experimental conditions: cellulose (1.0 g L<sup>-1</sup>), catalyst dosage (0.5 g L<sup>-1</sup>), PDS (1.2 g L<sup>-1</sup>). Scavenger concentration: p-BQ (200 mM), MeOH (10 mM), TBA (100 mM), L-Histidine (200 mM). (b) Quantification of active species in (NiCdCuFeCo)S<sub>x</sub>/PDS system. Experimental condition: catalyst dosage (0.1 g L<sup>-1</sup>), PDS (0.24 g L<sup>-1</sup>). Chemical probe concentration: FFA (50 μM), PHBA (2 mM), TA (480 μM), NBT (12 μM). (c) EPR spectra of generated active species in (NiCdCuFeCo)S<sub>x</sub>/PDS system. (d) The proposed reaction mechanism for the conversion of cellulose into CO over (NiCdCuFeCo)S<sub>x</sub>/PDS system.

photoluminescence (TA-PL) was used to measure the •OH concentration, [30] which was found to be only 2.3 μM. Furthermore, the combined amount of SO<sub>4</sub><sup>•-</sup> and •OH accounted for only 8% of the total active species (Fig. 3b, Fig. S23). The results were consistent with the weak signals of DMPO•OH and DMPO-SO<sub>4</sub><sup>•-</sup> observed in the electron paramagnetic resonance (EPR) spectra (Fig. 3c). These preliminary findings indicate a limited contribution of SO<sub>4</sub><sup>•-</sup> and •OH in the reaction system. Notably, the quenching experiments disclosed a significant inhibition of CO production by L-His scavenger, which serves as a quencher for <sup>1</sup>O<sub>2</sub> ( $k_{^1O_2, L-His} = 3.2 \times 10^7 \text{ M}^{-1} \text{ s}^{-1}$ ). This indicates the involvement of <sup>1</sup>O<sub>2</sub> in the photocatalytic reactions. Subsequent quantification of the generated <sup>1</sup>O<sub>2</sub> using furfuryl alcohol (FFA) as a probe [31–33] confirmed its abundant generation, with concentrations reaching up to 117 μM (Fig. 3b, Fig. S24). The EPR results also exhibited a stronger TEMP-<sup>1</sup>O<sub>2</sub> signal, further indicating substantial <sup>1</sup>O<sub>2</sub> generation in our reaction system (Fig. 3c). Despite L-His exhibited strong affinity for •OH ( $k_{\bullet OH, L-His} = 5 \times 10^9 \text{ M}^{-1} \text{ s}^{-1}$ ), the inappreciable inhibition effect of TBA scavenger suggests the quenching experiments by introducing L-His scavenger were still credible.[34].

The addition of p-benzoquinone (p-BQ) to serve as an O<sub>2</sub><sup>•-</sup> quencher ( $k_{O_2^{\bullet-}, p-BQ} = 0.9\text{--}1 \times 10^9 \text{ M}^{-1} \text{ s}^{-1}$ ) also inhibited CO generation to some extent. The concentration of O<sub>2</sub><sup>•-</sup> was quantified using nitroblue tetrazolium (NBT) and found to be only 7.7 μM (Fig. 3b, Fig. S25). The signal of the sextet EPR peak is observed in Fig. 3c. Nonradical reactions over metal sulfide can proceed through various pathways, including the generation of <sup>1</sup>O<sub>2</sub>, high-valent metal species, and surface-dependent electron transfer process (ETP). To confirm the presence of high-valent

metal species, methyl phenyl sulfoxide (PMSO) was added, [35] but no significant signal enhancement was observed for methyl phenyl sulfone (PMSO<sub>2</sub>), indicating the absence of high-valent metal species (Fig. S26). The negligible contribution of high-valent metal species to CO production is supported by the fact that lowering the solution pH, which typically stimulates the activity of high-valent metals in reaction system, had no promoting effect (Fig. S27). [36] In addition, the variation of the system current at a specific open-circuit voltage was recorded through electrochemical tests. [37–40] The observed weak intensity of the response indicates that the electron transfer pathway plays a negligible role in the reaction system, thus excluding the contribution of surface activated PDS\* (Fig. S28). Overall, these results imply that the <sup>1</sup>O<sub>2</sub> plays a key role in the conversion of cellulose. Both experimental results and theoretical calculations indicate that the interactions of the atoms in the HESS optimize the adsorption energy for PDS activation (Fig. S29–31). The electron gain and loss processes of (NiCdCuFeCo)S<sub>x</sub> along the atomic chain continuously convert PDS into abundant active species (<sup>1</sup>O<sub>2</sub>, O<sub>2</sub><sup>•-</sup>). Simultaneously, the light-driven thermal effect accelerates the electron gain and loss processes at high-entropy, generating more active species for the efficient and selective conversion of cellulose into value-added chemical feedstock CO (Fig. 3d). In order to understand the oxidative decomposition process of cellulose, gel permeation chromatography (GPC) was performed on the solutions before and after the cellulose reaction and after PDS activation, respectively, to elucidate the changes in molecular weight and molecular weight distribution. PDS activation reduces the molecular weight of cellulose to a certain extent (Fig. S32). The cellulose before and after

degradation was further collected and analyzed by infrared spectroscopy (FTIR) for changes in its molecular structure (Fig. S33).

### 3.4. Performance influencing factors

Owing to the chemically stable sulfur-cadmium ore structure of  $(\text{NiCdCuFeCo})\text{S}_x$  and the suitable reaction conditions, the  $(\text{NiCdCuFeCo})\text{S}_x$  catalyst exhibits excellent resistance to pH changes, high salinity, and environmental disturbances. The mild oxidation conditions are a result of the almost negligible generation of aggressive radicals and the abundant presence of non-radical  $^1\text{O}_2$  in the reaction system.  $(\text{NiCdCuFeCo})\text{S}_x$  is well stabilized with negligible changes in its crystal structure and electronic state before and after the reaction (Fig. S34–35). To further access the potential of  $(\text{NiCdCuFeCo})\text{S}_x$  in practical wastewater resource application, we investigated its performance in the presence of different background anions ( $\text{HCO}_3^-$ ,  $\text{NO}_3^-$ , and  $\text{SO}_4^{2-}$ ), varying pH values, and the addition of humic acid. Remarkably, the selectivity of cellulose conversion to CO remained above 95% even in the presence of various interfering substances (Fig. 4). Additionally,  $(\text{NiCdCuFeCo})\text{S}_x$  exhibits versatility across a wide pH range of 4.0–9.0, manifesting its applicability for a wide pH range of cellulose solutions. Fig. S36–39 demonstrate the effective conversion of actual toilet paper scraps and almost unaffected by common ions and natural organic matter in the wastewater. Based on GC, the main products were CO along with trace amounts of  $\text{C}_2\text{H}_4$  and  $\text{C}_2\text{H}_6$ . Nonradical  $^1\text{O}_2$ , a unique nonradical derivative of oxygen, is considered as one of the most promising reactive oxygen species. Its moderate oxidation potential, oxidation selectivity, long half-life, and strong resistance to interference make it an ideal pathway for oxidation. This effectively avoids the complete mineralization of renewable resources in the actual wastewater, allowing for the selective conversion of organic substances into high-value-added chemicals. These findings above highlight the immense potential of  $(\text{NiCdCuFeCo})\text{S}_x$  as a highly efficient catalyst for real domestic wastewater applications.

### 3.5. Environmental implication

Here, we propose a potential measure for domestic wastewater treatment that aims to reduce greenhouse gas emissions to the environment while achieving cost savings for municipal wastewater treatment plants. Building on the aforementioned findings, outdoor tests

were conducted using wastewater from the Shahe wastewater treatment plant in Yichang, China. A Fresnel lens was employed to concentrate sunlight onto a photocatalytic device. Since the use of a Fresnel lens with a larger area can in principle receives more light energy and thereby producing more products, we constructed a simple system that was operated with a circular photocatalyst area of 45 mm radius exposed to concentrated sunlight. The design and construction details of the outdoor photocatalytic device are depicted in Fig. 5a and b, and we further briefly compared the wastewater treatment plant process of this work with the domestic wastewater treatment process of an actual municipal wastewater plant (Fig. S40). Generally, a 345 mm  $\times$  345 mm Fresnel lens was utilized to concentrate sunlight and provide the necessary temperature for photocatalytic domestic wastewater conversion. The vessel opening of the photocatalytic reactor coincided with the focal point of the Fresnel lens, ensuring optimal utilization of solar energy. When natural light was concentrated to 2.5 suns,  $(\text{NiCdCuFeCo})\text{S}_x$  exhibited obvious bacterial removal rate from the real domestic wastewater (Fig. S41). In a 120-min outdoor test, the production yield of CO achieved a significant  $70 \mu\text{mol g}^{-1}$  (Fig. 5c), in which sunlight was harnessed to resourcefully convert macromolecular insoluble organic compounds in wastewater with similar kinetic conversion processes as the indoor photocatalytic reaction simulated by Xenon arc lamp. In this outdoor experiment, it is worth noting that the selectivity of CO is close to 100% (Fig. 5c, Fig. S42). The changes in system temperature due to solar irradiation were monitored in real time using an infrared thermal imager, while solar intensity fluctuations were measured with an optical power meter. The temperature of the reaction system increased from 27.6  $^\circ\text{C}$  to 44.7  $^\circ\text{C}$  after continuous irradiation of 15 min at the start of the experiment (Fig. S43). With the occasional cloud cover, there was some fluctuations in the temperature of the system. Throughout the 120-min outdoor test, the temperature and light intensity changes were recorded every 15 min, and the corresponding infrared thermal imaging images were captured (Fig. 5d, Fig. S44). The required reaction temperature was effectively achieved by harnessing previously unutilized infrared light from natural sunlight, indicating the efficient utilization of the potentials of  $(\text{NiCdCuFeCo})\text{S}_x$  catalyst. However, it should be noted that prolonged sunlight exposure may lead to inevitably loss of some catalysts, suggesting the need to address this issue and other associated challenges. Subsequently, inductively coupled plasma emission spectroscopy (ICP-AES) was used to analyze the relative leakage of each metal ion in the reaction solution. The average relative leaching rates of

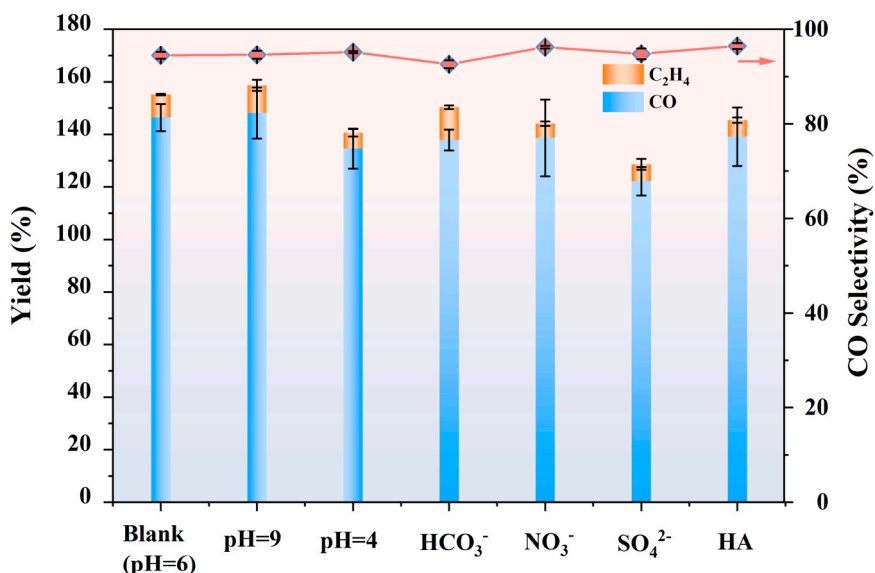
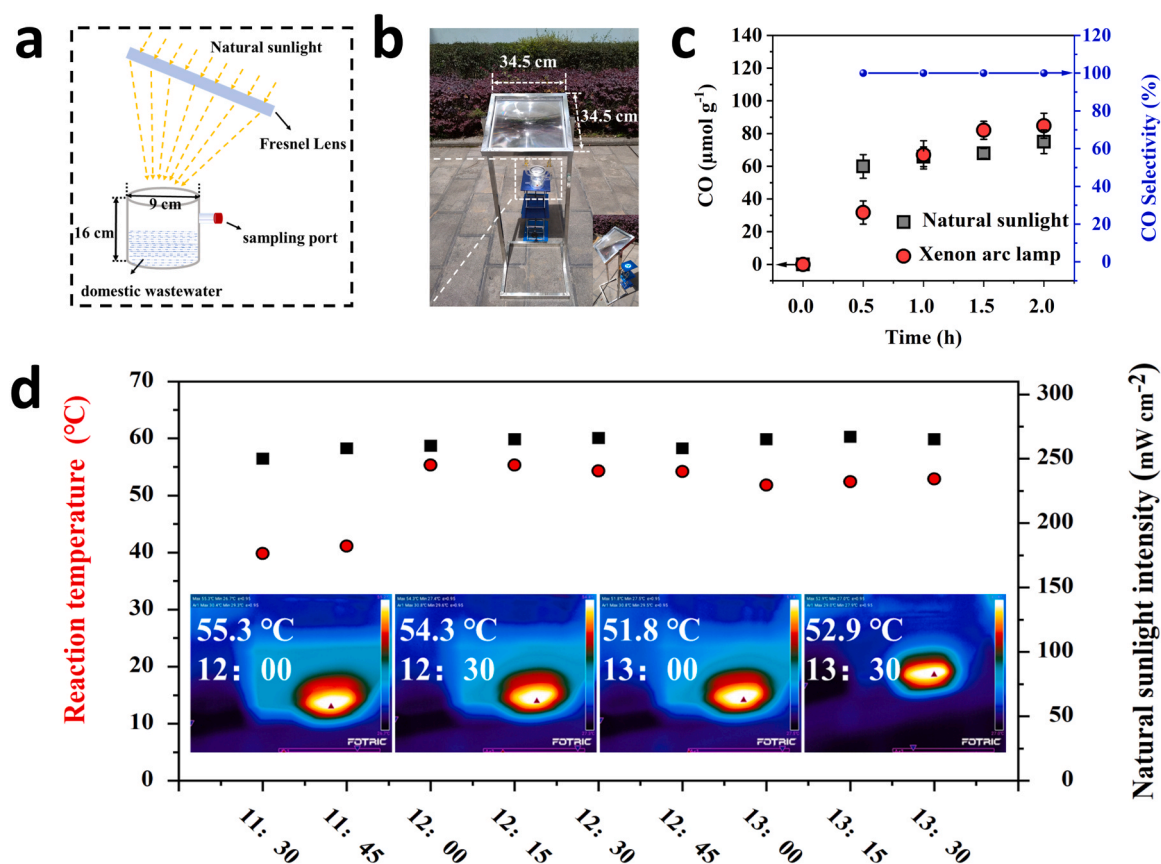


Fig. 4. The effects of concentrations of ions, humic acids, and pH on the yield and selectivity of cellulose conversion to CO. Experimental conditions: cellulose ( $1.0 \text{ g L}^{-1}$ ), catalyst dosage ( $0.5 \text{ g L}^{-1}$ ), PDS ( $1.2 \text{ g L}^{-1}$ ),  $\text{HCO}_3^-$  ( $2.4 \text{ mM}$ ),  $\text{SO}_4^{2-}$  ( $1.2 \text{ mM}$ ),  $\text{NO}_3^-$  ( $1.2 \text{ mM}$ ), HA ( $30 \text{ mg L}^{-1}$ ).



**Fig. 5.** Practical application of the process. (a) Schematic illustration of the set-up for an outdoor photocatalytic system for domestic wastewater conversion. (b) Image of the outdoor photocatalytic system that concentrates sunlight. The reaction took place at Three Gorges University in Yichang, Hubei province, China. (April 1, 2023, 3:00 pm to 5:00 pm,  $30^{\circ}43'29''\text{N}$ ,  $11^{\circ}18'42''\text{E}$ ). (c) Comparison of conversion of domestic wastewater to CO under Xenon arc lamp and natural sunlight (assisted by Fresnel lens solar condenser, the outdoor experiments were conducted at a concentrated intensity of  $250 \text{ mW cm}^{-2}$  to  $300 \text{ mW cm}^{-2}$ , with occasional cloud cover causing small fluctuations in light intensity). (d) The temperature change of the outdoor experimental system was recorded in real time using a thermal imaging camera, while the light intensity of the system was measured with an optical power meter. The outdoor experiment was performed on 31 May, 11:30 am to 13:30 pm. The weather was cloudy, outdoor high 29 degrees Celsius, low 20 degrees Celsius.

nickel, cadmium, copper, iron and cobalt in the reaction solution were 0.09, 0.26, 0.2, 0.378 and 0.06, respectively (Table S2). All in all, our study on the selective production of CO using domestic wastewater and inexhaustible sunlight as the resources serve as a potential solution to simultaneously address the global issues of imminent energy crisis and depletion of fossil fuels.

#### CRediT authorship contribution statement

Zhonglian Shi: Data curation, Formal analysis, Investigation, Writing – original draft. Chao Li: Data curation. Niu Huang: Data curation. Ziyi Jiang: Data curation. Li Wang: Data curation. Yingping Huang: Data curation, Funding acquisition, Xin Ying Kong: Data curation, Formal analysis. Po Keung Wong: Formal analysis. Liquan Ye: Conceptualization, Funding acquisition, Project administration, Supervision, Writing – review & editing.

#### Declaration of Competing Interest

The authors declare that they have no known competing financial interests or personal relationships that could have appeared to influence the work reported in this paper.

#### Data Availability

Data will be made available on request.

#### Acknowledgment

This work is supported by the National Natural Science Foundation of China (No. 22136003, 51872147), Hubei Provincial Natural Science Foundation of China (No. 2022CFA065), and the 111 Project (D20015).

#### Appendix A. Supporting information

Supplementary data associated with this article can be found in the online version at [doi:10.1016/j.apcatb.2023.123542](https://doi.org/10.1016/j.apcatb.2023.123542).

#### References

- [1] X. Hao, R. Liu, X. Huang, Evaluation of the potential for operating carbon neutral WWTPs in China, *Water Res* 87 (2015) 424–431.
- [2] L. Lu, J.S. Guest, C.A. Peters, X. Zhu, G.H. Rau, Z.J. Ren, Wastewater treatment for carbon capture and utilization, *Nat. Sustain* 1 (12) (2018) 750–758.
- [3] W.-J. Du, J.-Y. Lu, Y.-R. Hu, J. Xiao, C. Yang, J. Wu, B. Huang, S. Cui, Y. Wang, W.-W. Li, Spatiotemporal pattern of greenhouse gas emissions in China's wastewater sector and pathways towards carbon neutrality, *Nat. Water* 1 (2) (2023) 166–175.
- [4] D.R. Griffith, R.T. Barnes, P.A. Raymond, Inputs of fossil carbon from wastewater treatment plants to U.S. rivers and oceans, *Environ. Sci. Technol.* 43 (15) (2009) 5647–5651.
- [5] A.L. Smith, L.B. Stadler, L. Cao, N.G. Love, L. Raskin, S.J. Skerlos, Navigating wastewater energy recovery strategies: a life cycle comparison of anaerobic membrane bioreactor and conventional treatment systems with anaerobic digestion, *Environ. Sci. Technol.* 48 (10) (2014) 5972–5981.
- [6] W.-W. Li, H.-Q. Yu, B.E. Rittmann, Chemistry: reuse water pollutants, *Nature* 528 (7580) (2015) 29–31.

- [7] W.-W. Li, H.-Q. Yu, Z. He, Towards sustainable wastewater treatment by using microbial fuel cells-centered technologies, *Energy Environ. Sci.* 7 (3) (2014) 911–924.
- [8] J.-Y. Nam, M.D. Yates, Z. Zaybak, B.E. Logan, Examination of protein degradation in continuous flow, microbial electrolysis cells treating fermentation wastewater, *Bioresour. Technol.* 171 (2014) 182–186.
- [9] E.S. Heidrich, T.P. Curtis, J. Dolfing, Determination of the internal chemical energy of wastewater, *Environ. Sci. Technol.* 45 (2) (2011) 827–832.
- [10] J.P. Sumpter, A.C. Johnson, Lessons from endocrine disruption and their application to other issues concerning trace organics in the aquatic environment, *Environ. Sci. Technol.* 39 (12) (2005) 4321–4332.
- [11] N. Yan, K. Zhou, Y.W. Tong, D.T. Leong, M.P. Dickieson, Pathways to food from CO<sub>2</sub> via 'green chemical farming, *Nat. Sustain.* 5 (11) (2022) 907–909.
- [12] C.D. Scown, J.D. Keasling, Sustainable manufacturing with synthetic biology, *Nat. Biotechnol.* 40 (3) (2022) 304–307.
- [13] S. Oh, B.E. Logan, Hydrogen and electricity production from a food processing wastewater using fermentation and microbial fuel cell technologies, *Water Res.* 39 (19) (2005) 4673–4682.
- [14] M. Ran, H. Xu, Y. Bao, Y. Zhang, J. Zhang, M. Xing, Selective Production of CO from organic pollutants by coupling piezocatalysis and advanced oxidation processes, *Angew. Chem. Int. Ed.* 62 (22) (2023), e202303728.
- [15] W. Liu, P. Fu, Y. Zhang, H. Xu, H. Wang, M. Xing, Efficient hydrogen production from wastewater remediation by piezoelectricity coupling advanced oxidation processes, *Proc. Natl. Acad. Sci. U. S. A.* 120 (2023), e2218813120.
- [16] Z. Chen, F. An, Y. Zhang, Z. Liang, W. Liu, M. Xing, Single-atom Mo–Co catalyst with low biotoxicity for sustainable degradation of high-ionization-potential organic pollutants, *Proc. Natl. Acad. Sci.* 120 (29) (2023), e2305933120.
- [17] X.Y. Kong, Y.Y. Choo, S.-P. Chai, A.K. Soh, A.R. Mohamed, Oxygen vacancy induced Bi<sub>2</sub>WO<sub>6</sub> for the realization of photocatalytic CO<sub>2</sub> reduction over the full solar spectrum: from the UV to the NIR region, *Chem. Commun.* 52 (99) (2016) 14242–14245.
- [18] X. Mu, C. Li, L. Wang, R. Zhang, Y. Huang, X. Yu, P.K. Wong, L. Ye, Biosafe Bi<sub>2</sub>O<sub>2</sub>Se ultrathin nanosheet for water disinfection via solar-induced photothermal synergistic effect, *J. Hazard. Mater.* 440 (2022), 129808.
- [19] Y. Xu, L. Wang, Z. Shi, N. Su, C. Li, Y. Huang, N. Huang, Y. Deng, H. Li, T. Ma, X. Y. Kong, W. Lin, Y. Zhou, L. Ye, Peroxide-mediated selective conversion of biomass polysaccharides over high entropy sulfides via solar energy catalysis, *Energy Environ. Sci.* 16 (4) (2023) 1531–1539.
- [20] Y. Yao, Z. Huang, P. Xie, S.D. Lacey, R.J. Jacob, H. Xie, F. Chen, A. Nie, T. Pu, M. Rehwoldt, D. Yu, M.R. Zachariah, C. Wang, R. Shahbazian-Yassar, J. Li, L. Hu, Carbothermal shock synthesis of high-entropy-alloy nanoparticles, *Science* 359 (6383) (2018) 1489–1494.
- [21] K. Huang, B. Zhang, J. Wu, T. Zhang, D. Peng, X. Cao, Z. Zhang, Z. Li, Y. Huang, Exploring the impact of atomic lattice deformation on oxygen evolution reactions based on a sub-5 nm pure face-centred cubic high-entropy alloy electrocatalyst, *J. Mater. Chem. A.* 8 (24) (2020) 11938–11947.
- [22] Y. Yao, Q. Dong, A. Brozena, J. Luo, J. Miao, M. Chi, C. Wang, I.G. Kevrekidis, Z. J. Ren, J. Greeley, G. Wang, A. Anapolsky, L. Hu, High-entropy nanoparticles: Synthesis-structure-property relationships and data-driven discovery, *Science* 376 (6589) (2022), eabn3103.
- [23] C.R. McCormick, R.E. Schaak, Simultaneous multication exchange pathway to high-entropy metal sulfide nanoparticles, *J. Am. Chem. Soc.* 143 (2) (2021) 1017–1023.
- [24] C.J. Ruiken, G. Breuer, E. Klaversma, T. Santiago, M.C.M. van Loosdrecht, Sieving wastewater – cellulose recovery, economic and energy evaluation, *Water Res.* 47 (2013) 43–48.
- [25] M. Cui, C. Yang, B. Li, Q. Dong, M. Wu, S. Hwang, H. Xie, X. Wang, G. Wang, L. Hu, High-entropy metal sulfide nanoparticles promise high-performance oxygen evolution reaction, *Adv. Energy Mater.* 11 (3) (2021), 2002887.
- [26] J. Greeley, M. Mavrikakis, Alloy catalysts designed from first principles, *Nat. Mater.* 3 (11) (2004) 810–815.
- [27] Z.W. Seh, J. Kibsgaard, C.F. Dickens, I.B. Chorkendorff, J.K. Nørskov, T. F. Jaramillo, Combining theory and experiment in electrocatalysis: Insights into materials design, *Science* 355 (6321) (2017) ead4998.
- [28] L. Gao, Y. Guo, J. Zhan, G. Yu, Y. Wang, Assessment of the validity of the quenching method for evaluating the role of reactive species in pollutant abatement during the persulfate-based process, *Water Res.* 221 (2022), 118730.
- [29] Y. Zhao, M. Sun, Y. Zhao, L. Wang, D. Lu, J. Ma, Electrified ceramic membrane actuates non-radical mediated peroxymonosulfate activation for highly efficient water decontamination, *Water Res.* 225 (2022), 119140.
- [30] C. Hu, H. Huang, F. Chen, Y. Zhang, H. Yu, T. Ma, Coupling piezocatalysis and photocatalysis in Bi<sub>4</sub>NbO<sub>8</sub>X (X= Cl, Br) polar single crystals, *Adv. Funct. Mater.* 30 (2020), 1908168.
- [31] L.-S. Zhang, X.-H. Jiang, Z.-A. Zhong, L. Tian, Q. Sun, Y.-T. Cui, X. Lu, J.-P. Zou, S.-L. Luo, Carbon nitride supported high-loading Fe single-atom catalyst for activation of peroxymonosulfate to generate <sup>1</sup>O<sub>2</sub> with 100% selectivity, *Angew. Chem. Int. Ed.* 60 (40) (2021) 21751–21755.
- [32] N. Zheng, X. He, R. Hu, R. Wang, Q. Zhou, Y. Lian, Z. Hu, In-situ production of singlet oxygen by dioxygen activation on iron phosphide for advanced oxidation processes, *Appl. Catal. B Environ.* 307 (2022), 121157.
- [33] T. Liu, S. Xiao, N. Li, J. Chen, X. Zhou, Y. Qian, C.-H. Huang, Y. Zhang, Water decontamination via nonradical process by nanoconfined Fenton-like catalysts, *Nat. Commun.* 14 (1) (2023) 2881.
- [34] C. Zhao, L. Meng, H. Chu, J.-F. Wang, T. Wang, Y. Ma, C.-C. Wang, Ultrafast degradation of emerging organic pollutants via activation of peroxymonosulfate over Fe<sub>3</sub>C/Fe@N-C-x: singlet oxygen evolution and electron-transfer mechanisms, *Appl. Catal. B Environ.* 321 (2023), 122034.
- [35] M. Huang, Y. Li, C. Zhang, C. Cui, Q. Huang, M. Li, Z. Qiang, T. Zhou, X. Wu, H. Yu, Facilely tuning the intrinsic catalytic sites of the spinel oxide for peroxymonosulfate activation: From fundamental investigation to pilot-scale demonstration, *Proc. Natl. Acad. Sci. U. S. A.* 119 (2022), e2202682119.
- [36] H. Zhang, C.-H. Huang, Oxidative transformation of triclosan and chlorophene by manganese oxides, *Environ. Sci. Technol.* 37 (2003) 2421–2430.
- [37] Z. Guo, i SY, W. Xia, F. Wang, H. Liu, C. Yang, W. Li, Electron delocalization triggers nonradical Fenton-like catalysis over spinel oxides, *Proc. Natl. Acad. Sci. U. S. A.* 119 (2022), e2201607119.
- [38] W. Ren, C. Cheng, P. Shao, X. Luo, H. Zhang, S. Wang, X. Duan, Origins of electron-transfer regime in persulfate-based nonradical oxidation processes, *Environ. Sci. Technol.* 56 (1) (2022) 78–97.
- [39] Z. Guo, R. Sun, Z. Huang, X. Han, H. Wang, C. Chen, W. Li, Crystallinity engineering for overcoming the activity–stability tradeoff of spinel oxide in Fenton-like catalysis, *Proc. Natl. Acad. Sci. U. S. A.* 120 (2023), e2220608120.
- [40] Y.-H. Li, C.-C. Wang, F. Wang, W. Liu, L. Chen, C. Zhao, H. Fu, P. Wang, X. Duan, Nearly zero peroxodisulfate consumption for persistent aqueous organic pollutants degradation via nonradical processes supported by in-situ sulfate radical regeneration in defective MIL-88B(Fe), *Appl. Catal. B Environ.* 331 (2023), 122699.